Chiral materials to control exceptional points in parity-time-symmetric waveguides

Alice De Corte,[1,*] Mondher Besbes,[2] Henri Benisty,[2] and Bjorn Maes[1]
[1]Micro- and Nanophotonic Materials Group, Research Institute for Materials Science and Engineering, University of Mons, 20 Place du Parc, 7000 Mons, Belgium
[2]Laboratoire Charles Fabry, Institut d'Optique Graduate School, CNRS, Université Paris Saclay, 2 Avenue Augustin Fresnel, 91127 Palaiseau Cedex, France

(Received 20 October 2023; accepted 30 January 2024; published xxxxxxxxxx)

Parity-time ($\mathcal{PT}$) symmetry and chirality are both actively investigated in photonics due to the original behaviors they provide. We combine $\mathcal{PT}$ symmetry and chirality in a single photonic structure by inserting a chiral material in the narrow gap between $\mathcal{PT}$-symmetric coupled waveguides. We analyze the various effects of chiral coupling between the modes, especially in the vicinity of an exceptional point. By tuning the waveguide gap we tailor the chiral coupling between non-Hermitian modes with different polarizations, which would otherwise not interact. As a result, a rich variety of qualitatively differing dispersions is achieved, from typical anticrossings to symmetry-broken and associated symmetry-recovery zones, as well as a hybrid trimodal anticrossing. Furthermore, the slot effect in the gap leads to a very strong chiral coupling, reaching bulk sensitivity values near an exceptional point, which could be useful for sensing purposes. We employ a modified two-dimensional finite-element approach to include chirality in the simulations. Additionally, we propose a compact coupled-mode theory that elucidates the physics at play and provides opportunities for the study of more complex devices.

DOI: 10.1103/PhysRevA.00.003500

I. CONTEXT

Parity-time ($\mathcal{PT}$) symmetry is extensively studied in photonic structures, with various implementations in waveguides [1–4], lattices and metasurfaces [5–7], plasmonics [8,9], and several other possibilities [10–15]. An essential approach is via two coupled waveguides of identical geometry with a balanced imaginary part of the refractive index, thus one with a photonic gain material and the other with an equal amount of loss [1,8,11,13]. Typically, $\mathcal{PT}$-symmetric waveguides operate in two separate regimes, depending on the value of the gain-loss parameter γ. The transition between these two regimes occurs at the exceptional point (EP), at a certain value γ_{EP} dependent on the mode coupling via optogeometric parameters. In the $\mathcal{PT}$-symmetric regime $\gamma < \gamma_{\mathrm{EP}}$, both supermodes of the structure propagate without any gain or loss, whereas in the $\mathcal{PT}$-broken regime $\gamma > \gamma_{\mathrm{EP}}$, one supermode benefits from gain and increases in amplitude, while the other experiences loss and exponentially decays [14,16,17].

As regards chirality, for the case of plane waves propagating in a uniform medium, it is well known that a chiral material rotates the polarization plane, a phenomenon called optical activity that has been known since Pasteur [18]. Used mostly for enantiomer detection in chemistry and biology [19], these techniques are based on the different response to left-handed and right-handed circularly polarized light [20–23]. Various types of chirality have since been implemented and utilized in photonic structures [19,24,25]. In particular, waveguide systems with chiral materials were studied [26–29] and chirality was combined with EPs in ring resonators [30–32].

It was also shown that chirality and $\mathcal{PT}$ symmetry are related in several ways: $\mathcal{PT}$ symmetry can be implemented in a bulk material as an electrical anisotropy to induce a chiral polarization in the states of the system stemming only from $\mathcal{PT}$ symmetry [33]. Additionally, such bulk $\mathcal{PT}$ symmetry can be studied in combination with material chirality to gain insight into the polarization dependence around the EP, as well as creating directionality [34]. Furthermore, chirality was implemented in $\mathcal{PT}$-symmetric metamaterials, on the one hand as a way to break $\mathcal{PT}$ symmetry in polarization space [35] and on the other hand to conserve $\mathcal{PT}$ symmetry in scattering multilayers [36–38]. Finally, it was recently shown that $\mathcal{PT}$ symmetry can enhance chiral sensing with a multilayer approach [39]. However, the influence of material chirality on the eigenstates of $\mathcal{PT}$-symmetric coupled waveguides has not been discussed yet, in spite of the importance of these photonic elements for many applications.

In this work we place a chiral material in the gap between $\mathcal{PT}$-symmetric coupled waveguides. We study the rich influence of chirality on the system's supermodes by numerical means and propose a coupled-mode theory that elucidates in detail the salient features: the dispersion, including the EP-related singularities, the mode profiles, and the polarization. Different types of avoided crossings can be obtained in the chiral mode dispersion by tuning the size of the gap. For narrow gaps, an anticrossing appears between quasi-TE and quasi-TM modes of the same parity. These modes are linearly polarized in the absence of chirality, but they become

*alice.decorte@umons.ac.be

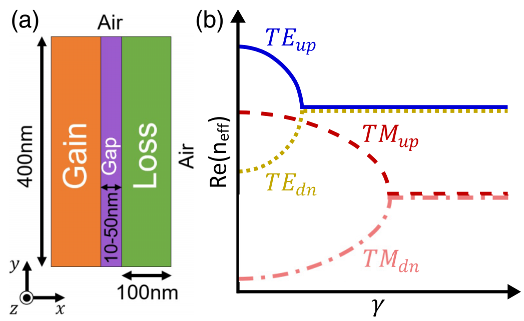

FIG. 1. $\mathcal{PT}$-symmetric rectangular waveguides (orange and green) and chiral gap (purple), with mode propagation in the z direction. The device is embedded in air. (b) Schematic of typical TE (blue solid line and gold dotted line) and TM (red dashed line and pink dash-dotted line) real dispersions of the structure as a function of the gain-loss parameter γ. The subscripts up and dn refer to the upper and lower branches of the $\mathcal{PT}$ forks for each polarization.

quasicircularly polarized with chirality. For wider gaps, a crossing occurs in the dispersion between quasi-TE and quasi-TM modes of opposite parity. This causes the uncommon appearance of a $\mathcal{PT}$-broken zone in the previously $\mathcal{PT}$-symmetric phase, followed by symmetry recovery with an inverted EP. As explained with the theoretical model, this feature requires balanced gain and loss. In the locally $\mathcal{PT}$-broken zone, the polarization of the modes becomes suddenly linear. A specific intermediate situation arises for medium-size gaps, where the dispersion crossing occurs right at the EP. Chirality then yields a trimodal anticrossing effect that appears to reach the same sensitivity as a fully homogeneous chiral medium, in tight connection with the field enhancement in the slot.

This paper is structured as follows. In Sec. II the $\mathcal{PT}$-symmetric coupled waveguide structure is described. The various types of avoided crossings generated by chirality are studied in Sec. III by employing a finite-element method that embeds chirality in the constitutive relations. In Sec. IV the coupled-mode theory describing our system is presented. In Sec. V the mode profiles and their polarization are examined in detail. We summarize in Sec. VI.

II. DEVICE GEOMETRY AND NUMERICAL APPROACH

Our structure is composed of two $\mathcal{PT}$-symmetric waveguides with a rectangular cross section, with an aspect ratio of 4 chosen in order to obtain the desired TE-TM degeneracy (discussed later). Though other aspect ratios (e.g., 3) can also produce these degeneracies, we find that a value of 4 gives dispersions that are easier to tune in the context of our study. One waveguide is made of a gain material and the other has loss [Fig. 1(a)]. A potentially chiral material (without gain or loss) is located in the narrow gap between them. We employ a waveguide width of 100 nm and thickness of 400 nm, for a vacuum wavelength of 350 nm (but the phenomena can be rescaled to other sizes and wavelengths). The gap width between the waveguides varies between 10 and 50 nm. The gain and loss materials are characterized by refractive indices of $2 - i\gamma$ and $2 + i\gamma$, respectively, so γ, the gain-loss parameter, is here the imaginary part of the refractive index (not to be confused with an effective, integrated coefficient). The gap material can possess a nonzero chirality parameter κ defined via the chiral constitutive relations [37]

$$\vec{D} = \varepsilon\vec{E} + i\frac{\kappa}{c}\vec{H}, \quad \vec{B} = \mu\vec{H} - i\frac{\kappa}{c}\vec{E}, \tag{1}$$

where $\vec{D}$ and $\vec{E}$ are the electric displacement and field, respectively, $\vec{B}$ and $\vec{H}$ are the magnetic induction and field, respectively, $\varepsilon = \varepsilon_0\varepsilon_r$ (with ε_0 and ε_r the vacuum and relative electric permittivity, respectively), $\mu = \mu_0\mu_r$ (with μ_0 and μ_r the vacuum and relative magnetic permeability, respectively), c is the speed of light in vacuum, and i is the imaginary number.

We use the mode solver of the SIMPHOTONICS MATLAB toolbox, a Maxwell equation solver developed at Laboratoire Charles Fabry to simulate our setup. SIMPHOTONICS was upgraded to enable finite-element method (FEM) modeling based on the generalized Helmholtz equation in the case of chiral media,

$$\begin{aligned} &\vec{\nabla} \times (p\vec{\nabla} \times \vec{U}) - k_0\vec{\nabla} \times (\kappa p\vec{U}) - k_0^2(q - \kappa^2 p)\vec{U} \\ &\quad - k_0\kappa p\vec{\nabla} \times \vec{U} = 0, \end{aligned} \tag{2}$$

where p, q, $\vec{U}$, and κ are all functions of space and k_0 is the vacuum wave vector. In the electric formulation $p = \frac{1}{\mu_r}$, $q = \varepsilon_r$, and $\vec{U} = \vec{E}$, while in the magnetic formulation $p = \frac{1}{\varepsilon_r}$, $q = \mu_r$, and $\vec{U} = \vec{H}$. For a homogeneous medium (p, q, and κ constant), Eq. (2) shows that chirality introduces a single-derivative term $-2k_0\kappa p\vec{\nabla} \times \vec{U}$ as well as adding a contribution $k_0^2\kappa^2 p\vec{U}$ to the nonderived term.

The devices described in this paper could be experimentally realized. The gain-loss parameter γ we employ is on the order of 0.1. This is relatively high compared to common experimental values that are usually on the order of 0.01 for crystalline semiconductors in commercial optical amplification technology, but such high values can be obtained through careful engineering of the photonic structure [5]. Additionally, the geometry of our structure can be adjusted by widening the gap (lowering the coupling) and adapting the waveguide aspect ratio accordingly so that the desired dispersion features (such as the EP) shift to lower values of gain and loss for more feasible experiments. The chirality parameter κ, here set to 0.012, is large compared to naturally occurring chiral materials. However, chirality parameters on the order of 0.01 are reported for chiral liquids [40,41], and metamaterials can exhibit even stronger chirality [42–44]. Finally, the effects also appear for smaller κ: The anticrossings and broken zones become narrower as κ decreases, but there is no threshold value.

III. CHIRALITY-INDUCED AVOIDED CROSSINGS

In this section we assess the effect of chirality on the $\mathcal{PT}$ mode dispersion obtained by FEM calculations. As the structure is two dimensional, quasi-TE and quasi-TM modes coexist in the achiral case. We refer to the modes with a dominant y electric-field component as quasi-TE and the modes with a dominant y magnetic-field component as quasi-TM. Due to the double-waveguide symmetry of the structure, a symmetric mode and an antisymmetric mode form the

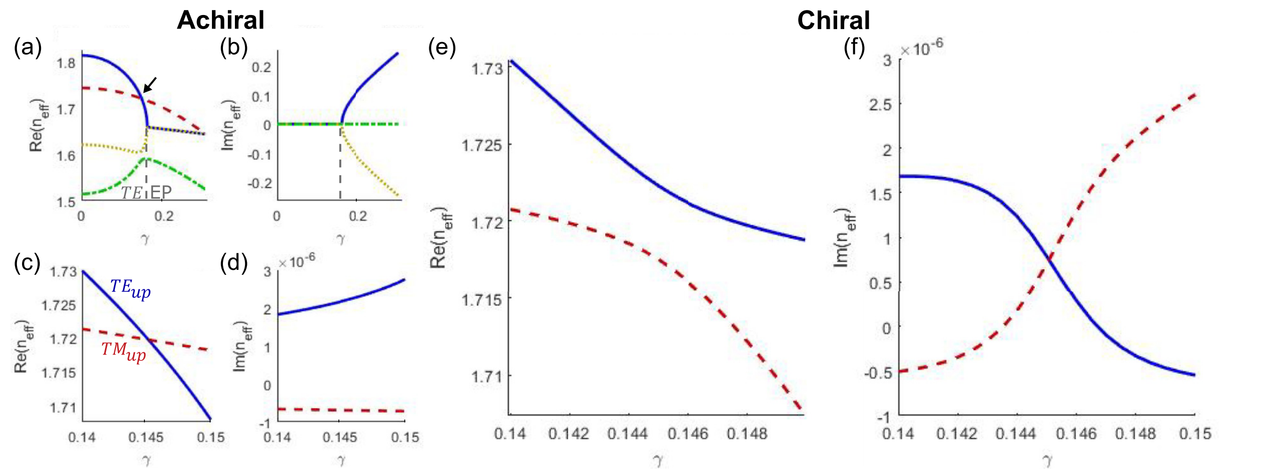

FIG. 2. (a) Real and (b) imaginary effective indices for the four highest index modes of the 12-nm-gap structure without chirality. Dispersion of modes TE_{up} (blue solid line) and TM_{up} (red dashed line) around their crossing for a 12-nm-thick gap are shown for (c) and (d) achiral and (e) and (f) chiral materials. The black arrow in (a) indicates the relevant crossing, which is enlarged in (c).

fundamental $\mathcal{PT}$ fork for each polarization. A schematic of a typical dispersion is represented in Fig. 1(b), with the TE fork represented by blue solid and gold dotted curves, while the red dashed and pink dash-dotted curves show the TM fork. The parity is indicated via the subscripts: We employ the subscript up to refer to modes that have symmetric transverse components at $\gamma = 0$ (blue solid line and red dashed line) and the subscript dn to refer to modes with antisymmetric transverse components at $\gamma = 0$ (gold dotted line and pink dash-dotted line), transverse meaning H_x and E_y for TE modes and E_x and H_y for TM modes. Without chirality, these two forks do not interact and remain independent.

The chirality parameter κ is set to 0.012 in all chiral simulation results shown in this paper. The chiral modes are also referred to using $TE,TM_{up,dn}$ abbreviations by analogy with the achiral modes, since the order of the modes in the dispersion generally remains the same, with the exception of the chirality-induced avoided crossings, as discussed later.

The structure is designed such that, depending on the gap width, the TM_{up} dispersion crosses the TE fork at a specific place: through the upper part TE_{up}, through the lower part TE_{dn}, or precisely at the TE EP. For a narrow gap, e.g., 12 nm [see Fig. 2(a)], TM_{up} (red dashed line) crosses TE_{up} (blue solid line) for a value $\gamma < \gamma_{EP}$. As the gap width increases, conventional (achiral) coupling decreases, resulting in a lower value of γ_{EP} and a lower position of the TM_{up} crossing within the TE fork. For wide gaps, e.g., 44 nm [see Fig. 3(a)], a crossing occurs between TM_{up} and TE_{dn} (gold dotted line). For medium-width gaps, e.g., 32 nm [see Fig. 4(a)], crossing occurs right at the quasi-TE EP. Now when chirality is introduced in the gap, the modal dispersion picture is qualitatively altered, primarily around these crossings, with the appearance of an anticrossing for narrow gaps, a $\mathcal{PT}$-broken zone for wide gaps, and a hybrid trimodal anticrossing for medium gaps, as discussed in the following.

We note that the avoided crossings in this section assume that κ is real. For imaginary κ the effects are interchanged: A $\mathcal{PT}$-broken zone appears for narrow gaps (crossing the upper TE branch) while an anticrossing emerges for large gaps (crossing the lower TE branch). Furthermore, the avoided crossings acquire a hybrid nature when κ is complex as both effects compete in altering the dispersion, without new emerging phenomena; more information is provided in Appendix A.

A. Anticrossing

For narrow gaps, the dispersion of mode TM_{up} crosses the TE $\mathcal{PT}$ fork above the TE EP, located around $\gamma = 0.16$ [see Figs. 2(a) and 2(b)] (negligible imaginary index for $\gamma < \gamma_{EP}$), with a focus on the crossing area in Figs. 2(c) and 2(d). Two modes having the same parity symmetry and thus cross dispersions (TM_{up} and TE_{up} here, with symmetric profiles along x) without chirality [Figs. 2(c) and 2(d)]. Subsequently, chirality splits the effective indices into two values: The dispersion curves [Fig. 2(c)] spread apart around the crossing [Fig. 2(e)], while remaining real, as $\mathrm{Im}(n_{eff})$ is negligible [Fig. 2(f)]. This is expected; chirality lifts the TE-TM degeneracy, much as it does in the bulk, or in chirally loaded waveguides [26] whenever accidental crossings occur. Here the main function of the gain-loss parameter is thus to create degeneracies among certain branches, which are not available in lossless situations.

The size of the anticrossing, i.e., the splitting between the effective indices of the modes, increases linearly with the chirality of the gap material. This situation is essentially similar to optical activity observed in bulk chiral media, where the effective indices of right and left circularly polarized waves are $n_{RCP} = n + \kappa$ and $n_{LCP} = n - \kappa$, respectively, with n the bulk refractive index. This similarity will also be evidenced in Sec. V when discussing the polarization of the chiral modes.

B. Local symmetry breaking

For broad enough gaps, both forks get narrower so the dispersion of mode TM_{up} crosses the TE $\mathcal{PT}$ fork under its EP, located in our example around $\gamma = 0.09$ [see Figs. 3(a) and 3(b) as well as the close-ups in Figs. 3(c) and 3(d)]. Two modes of different parity thus become degenerate: TM_{up} with a symmetric profile and TE_{dn} with an antisymmetric profile along x (red dashed line and gold dotted line in Fig. 3).

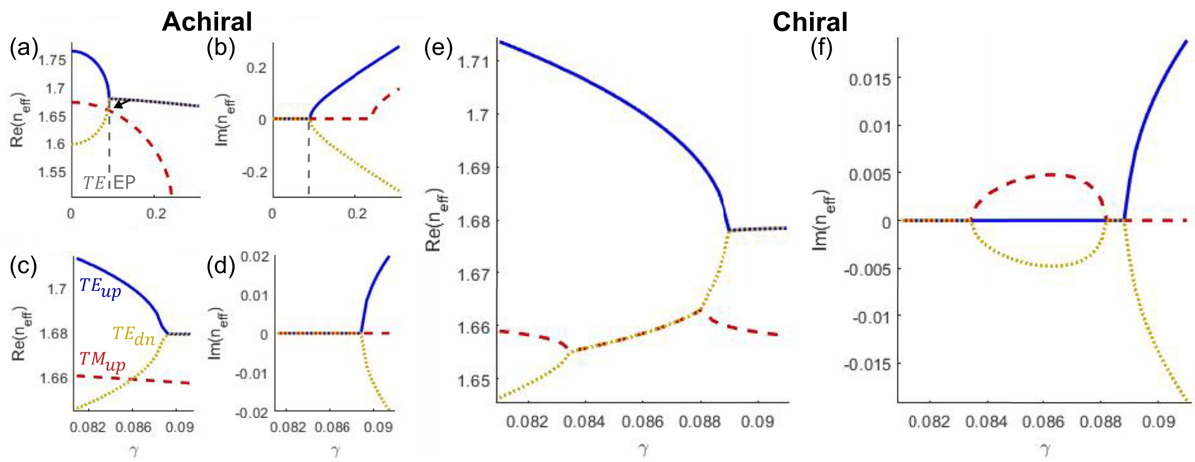

FIG. 3. (a) Real and (b) imaginary dispersions of modes TE_{up} (blue solid line), TM_{up} (red dashed line), and TE_{dn} (gold dotted line) of the 44-nm-gap structure without chirality. The same dispersions around the mode crossing for a 44-nm-thick gap are shown for (c) and (d) achiral and (e) and (f) chiral materials. The black arrow in (a) indicates the relevant crossing, which is enlarged in (c).

Intriguingly, chirality induces the appearance of a $\mathcal{PT}$-broken zone in the $\mathcal{PT}$-symmetric regime around the crossing [0.083–0.088 in Figs. 3(e) and 3(f)]. The effective indices of the modes present equal real parts [Fig. 3(e)] and acquire a substantial imaginary part [Fig. 3(f)], despite γ being below γ_{EP} for both forks. At both ends of the locally broken "bubble" there are thus two new exceptional points, one on the left with the usual topology (from real to imaginary) and one on the right with the inverted topology (from imaginary to real, which can be called symmetry recovery).

The width and magnitude of the local symmetry-breaking zone increase linearly with the chirality of the gap material; thus the $\mathcal{PT}$-symmetry breaking is due to the chiral coupling. Local symmetry breaking followed by symmetry recovery has already been observed, e.g., in the somewhat more intricate case of four-waveguide systems [45], but here chirality offers the same possibility with only two waveguides by allowing quasi-TE and quasi-TM modes to couple. We will see later that the gain and loss in this system are essential to be able to break the symmetry locally; this is not possible in a passive, lossless system (unlike the anticrossing of the preceding section).

C. Trimodal anticrossing

At the TE EP, TE_{up} and TE_{dn} modes coalesce: In addition to having the same propagation constant, their field profiles are the same instead of being orthogonal. For a medium gap width, the TM_{up} dispersion [red dashed lines in Figs. 4(a) and 4(b)] crosses the TE fork exactly at the EP [close-ups in Figs. 4(c) and 4(d)] and thus interacts with both TE modes (blue solid line and gold dotted line), resulting in a hybrid coupling. The dispersions of TM_{up} and TE_{up} seem to undergo an anticrossing: The blue solid curve and red dashed curve spread apart in Fig. 4(e), while the real dispersions of TM_{up} (red dashed line) and TE_{dn} (gold dotted line) join together in an EP. Through this process the EP is slightly shifted towards lower values of γ [Fig. 4(f)] and the $\mathcal{PT}$-broken regime is attained earlier: The imaginary part becomes nonzero at $\gamma = 0.110$ in the achiral case, but at $\gamma < 0.109$ with chirality.

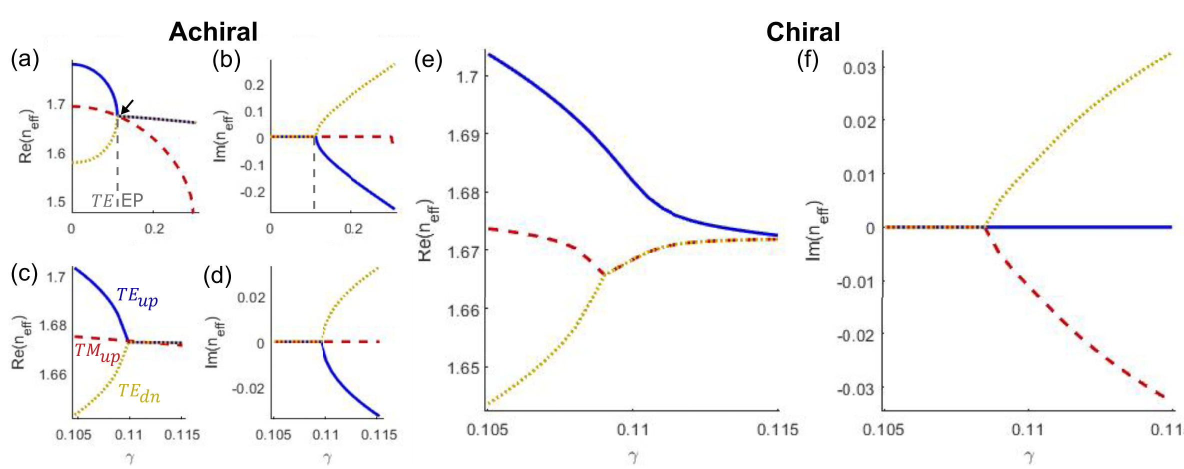

FIG. 4. (a) Real and (b) imaginary dispersions of modes TE_{up} (blue solid line), TM_{up} (red dashed line), and TE_{dn} (gold dotted line) of the 32-nm-gap structure without chirality. The same dispersions around the mode crossing for a 32-nm-thick gap are shown for (c) and (d) achiral and (e) and (f) chiral materials. The black arrow in (a) indicates the relevant crossing, which is enlarged in (c).

The size of the anticrossing, measured vertically between the shifted EP [junction between red dashed and gold dotted curves in Fig. 4(e)] and the first chiral mode (blue line), increases linearly with the chirality of the gap material, with a proportionality coefficient that is close to the Pasteur value in the case of bulk medium splitting. There is thus a potential for a large sensitivity enhancement, which we attribute to field enhancement in the narrow gap or slot between the waveguides, as this highly localized, partial modal overlap (discussed later) leads to the same chiral coupling as bulk plane waves.

We note that this EP remains a degeneracy between two modes despite the effect of chirality; it is therefore not a higher-order EP. The combination of higher-order EPs and chirality in this type of design is a topic for further study, which could be implemented, e.g., using coupled ring cavities with chiral waveguides, extending the structures in [46].

IV. COUPLED-MODE THEORY

We have derived a coupled-mode model that accounts for the patterns evidenced in the preceding section and other effects. In coupled $\mathcal{PT}$ waveguides without chirality, the isolated modes in each separate waveguide (gain and loss) are assumed to have the same polarization in order to couple into supermodes, either (quasi-)TE or (quasi-)TM [1]. The addition of a chiral material in the gap offers a way to couple TE and TM modes, through interaction of the electric and magnetic fields [see Eq. (1)], thereby adding a coupling channel between the two waveguides. To model this interaction, the "standard" $\mathcal{PT}$ coupled equations must be supplemented by a coupling between the polarizations. The resulting system can be written in matrix form, in the basis of the isolated waveguide modes, as

$$\frac{i}{k_0}\frac{d}{dz}\begin{bmatrix}\mathrm{TE}_g\\ \mathrm{TE}_l\\ \mathrm{TM}_g\\ \mathrm{TM}_l\end{bmatrix}=\begin{bmatrix} n_{\mathrm{TE}}-i\gamma_{\mathrm{TE}} & C_{\mathrm{TE}} & \beta & \alpha\\ C_{\mathrm{TE}} & n_{\mathrm{TE}}+i\gamma_{\mathrm{TE}} & \alpha & \beta\\ \beta^* & \alpha^* & n_{\mathrm{TM}}-i\gamma_{\mathrm{TM}} & C_{\mathrm{TM}}\\ \alpha^* & \beta^* & C_{\mathrm{TM}} & n_{\mathrm{TM}}+i\gamma_{\mathrm{TM}}\end{bmatrix}\begin{bmatrix}\mathrm{TE}_g\\ \mathrm{TE}_l\\ \mathrm{TM}_g\\ \mathrm{TM}_l\end{bmatrix}, \tag{3}$$

where g refers to the gain waveguide [left in Fig. 1(a)] and l to the lossy waveguide [right in Fig. 1(a)], n_{TE} and n_{TM} are the effective indices of the isolated TE and TM modes (without any coupling), and C_{TE} and C_{TM} are the coupling constants from conventional directional coupler theory (from the left TE-TM mode to the right TE-TM mode and vice versa). The effective imaginary refractive indices perceived by the isolated TE and TM modes, γ_{TE} and γ_{TM}, are proportional to the material imaginary refractive index γ by a confinement factor dependent on the polarization (more details in Appendix B). In the off-diagonal subblocks, α and β determine the new chiral coupling when a chiral material is in the gap, detailed further on, which are proportional to κ.

It is instructive to write the matrix of Eq. (3) in the basis of the four achiral $\mathcal{PT}$ supermodes $\mathrm{TE_{up}}$, $\mathrm{TE_{dn}}$, $\mathrm{TM_{up}}$, and $\mathrm{TM_{dn}}$ (the eigenmodes of the traditionally coupled but achiral waveguides). If we consider $C_{\mathrm{TE}}=C_{\mathrm{TM}}=C$ and $\gamma_{\mathrm{TE}}=\gamma_{\mathrm{TM}}=\gamma$ for brevity and simplicity, the supermode coupling matrix is given by

$$M_{\mathrm{sm}}=\begin{bmatrix} n_{\mathrm{TE}}+A & 0 & \frac{\beta A+C\alpha}{A} & \frac{\alpha\gamma}{CA}(\gamma+iA)\\ 0 & n_{\mathrm{TE}}-A & \frac{\alpha\gamma}{C}(-\gamma+iA) & \frac{\beta A-C\alpha}{A}\\ \frac{\beta^*A+C\alpha^*}{A} & \frac{\alpha^*\gamma}{CA}(\gamma+iA) & n_{\mathrm{TM}}+A & 0\\ \frac{\alpha^*\gamma}{CA}(-\gamma+iA) & \frac{\beta^*A-C\alpha^*}{A} & 0 & n_{\mathrm{TM}}-A\end{bmatrix}, \tag{4}$$

where the quantity $A=\sqrt{C^2-\gamma^2}$ is characteristic of the $\mathcal{PT}$ mode dispersion.

This form (4) elucidates distinct features of the coupling between same-symmetry and opposite-symmetry TE and TM modes (with respect to parity). Indeed, isolating the matrix coefficients that link $\mathrm{TE_{up}}$ and $\mathrm{TM_{up}}$ (selecting lines and columns 1 and 3) gives the subblock matrix

$$M_{\mathrm{up,up}}=\begin{bmatrix} n_{\mathrm{TE}}+A & \frac{\beta A+C\alpha}{A}\\ \frac{\beta^*A+C\alpha^*}{A} & n_{\mathrm{TM}}+A\end{bmatrix}. \tag{5}$$

Its eigenvalues in the case of the $\mathrm{TE_{up}}$-$\mathrm{TM_{up}}$ crossing ($n_{\mathrm{TE}}+A=n_{\mathrm{TM}}+A$) are $n_{\mathrm{TE}}+A\pm\frac{|\beta A+C\alpha|}{A}$ and are therefore real, which characterizes the splitting or anticrossing under the effect of chirality (as in Sec. III A). This is due to the product of the chiral (antidiagonal) terms of matrix $M_{\mathrm{up,up}}$ [Eq. (5)] being positive.

The same process for a $\mathrm{TE_{dn}}$ and $\mathrm{TM_{up}}$ mode pair [selecting lines and columns 2 and 3 in Eq. (4)] gives the matrix

$$M_{\mathrm{dn,up}}=\begin{bmatrix} n_{\mathrm{TE}}-A & \frac{\alpha\gamma}{CA}(-\gamma+iA)\\ \frac{\alpha^*\gamma}{CA}(\gamma+iA) & n_{\mathrm{TM}}+A\end{bmatrix}. \tag{6}$$

Its eigenvalues at the $\mathrm{TE_{dn}}$-$\mathrm{TM_{up}}$ crossing ($n_{\mathrm{TE}}-A=n_{\mathrm{TM}}+A$) are $n_{\mathrm{TE}}-A\pm\frac{i|\alpha|\gamma}{A}$ and are therefore complex, characterizing the locally $\mathcal{PT}$-broken zone brought about by chirality (the bubble in Sec. III B). This is due to the product of the chiral (antidiagonal) terms of matrix $M_{\mathrm{dn,up}}$ [Eq. (6)] now being negative.

For the system without gain and loss, $\gamma=0$, Eq. (4) becomes

$$M_{\mathrm{sm}}=\begin{bmatrix} n_{\mathrm{TE}}+C & 0 & \beta+\alpha & 0\\ 0 & n_{\mathrm{TE}}-C & 0 & \beta-\alpha\\ \beta^*+\alpha^* & 0 & n_{\mathrm{TM}}+C & 0\\ 0 & \beta^*-\alpha^* & 0 & n_{\mathrm{TM}}-C\end{bmatrix}. \tag{7}$$

TABLE I. Effective indices, couplings, and confinement factors of isolated TE and TM modes for structures with 12-, 32-, and 44-nm-wide achiral gaps.

	TE			TM		
Gap (nm)	n	C	F	n	C	F
12	1.664	0.149	0.937	1.517	0.226	0.695
32	1.678	0.101	0.916	1.526	0.167	0.571
44	1.680	0.0834	0.937	1.525	0.148	0.626

TABLE II. Chiral couplings calculated from mode overlap integrals at $\gamma = 0$ for structures with 12-, 32-, and 44-nm-wide achiral gaps.

Gap (nm)	α	β
12	$0.0320i$	$0.0682i$
32	$0.0512i$	$0.1370i$
44	$0.0610i$	$0.1566i$

The zeros in this system demonstrate that coupling between modes of opposite symmetry (leading to the locally broken zone) is impossible without $\mathcal{PT}$ symmetry in this configuration. As indicated before, gain and loss are thus genuinely required to achieve the local symmetry-breaking zone presented in Sec. III B and are not just a tuning mechanism to obtain degeneracy.

We can recreate the avoided crossings observed in the simulations via the eigenvalues of the coupling matrix in either basis [isolated modes (3) or supermodes (4)]. First, we obtain the achiral parameters n_{TE}, n_{TM}, C_{TE}, and C_{TM} using the simulated achiral dispersion (their values are included in Table I of Appendix B). Second, the chiral coupling coefficients α and β are calculated using an overlap integral over the gap area and the supermode profiles at $\gamma = 0$. Chiral coupling between supermodes was discussed in [26], leading to

$$I_{mn} = i \iint_S \omega \frac{\kappa}{c} (\vec{H}_n^* \cdot \vec{E}_m - \vec{E}_n^* \cdot \vec{H}_m) dS, \tag{8}$$

where the subscripts n and m designate supermodes of the achiral structure, ω is the mode frequency, and S is the surface of the chiral gap. The modes in Eq. (8) are normalized by their overlap integral over the whole simulation domain $\iint_S (\vec{E}_m \times \vec{H}_n^* + \vec{E}_n^* \times \vec{H}_m) \cdot \hat{z}\, dS = \delta_{mn}$. The chiral overlap integrals, when calculated using the supermode profiles at $\gamma = 0$, are directly related to the chiral coupling coefficients of Eq. (7): $\beta + \alpha$ and $\beta - \alpha$. Coefficients α and β can thus be obtained from these integrals, as explained in more detail in Appendix B. The calculated values of α and β are included in Table II in Appendix B. The resulting eigenvalue dispersions are shown in Fig. 5, showing an accurate match to the simulations, especially considering that we calculate the chiral coupling at the simplest, lossless situation ($\gamma = 0$) and apply it for all γ values.

We note that the model and dispersions in this section assume the chirality parameter κ to be real. For complex or imaginary κ, the model requires a slight adjustment: The overlap integrals [Eq. (8)] that enable the calculation of chiral couplings α and β verify $I_{mn} = I_{nm}^*$ if κ is real, whereas for a complex κ we get $I_{mn} = \frac{\kappa}{\kappa^*} I_{nm}^* = e^{2i\phi(\kappa)} I_{nm}^*$, where $\phi(\kappa)$ is the phase of κ. The chiral couplings α and β then become complex instead of imaginary and α^* and β^* in Eq. (3) must be multiplied by $e^{2i\phi(\kappa)}$. These adjustments influence the effects as discussed in Sec. III and as shown in simulated dispersions in Appendix A.

V. MODE PROFILES

It is interesting to view the chirality effect through the mode profiles and polarizations. Electric-field profiles of relevant modes, as well as their polarization at the center of the gap (at $x = y = 0$), are presented below. Magnetic-field profiles of the corresponding modes are included in Appendix C.

A. Anticrossing

In addition to lifting the degeneracy at the crossing between modes $\mathrm{TE_{up}}$ and $\mathrm{TM_{up}}$, chirality couples these modes to form two quasicircular polarization modes at the anticrossing. Figures 6(a) and 6(b) show the profiles and polarization, respectively, of the achiral $\mathrm{TE_{up}}$ mode, with a clearly dominant y electric-field component, highlighting its quasi-TE nature. Figures 6(c) and 6(d) show the profiles and polarization of the anticrossing's highest-index mode in the presence of chirality, which we also call $\mathrm{TE_{up}}$ by analogy. The x and y electric-field components have similar amplitudes in the gap; the x component presents a strong slot effect due to its perpendicularity to the gap (via continuity of the normal $\vec{D}$ component) [47,48].

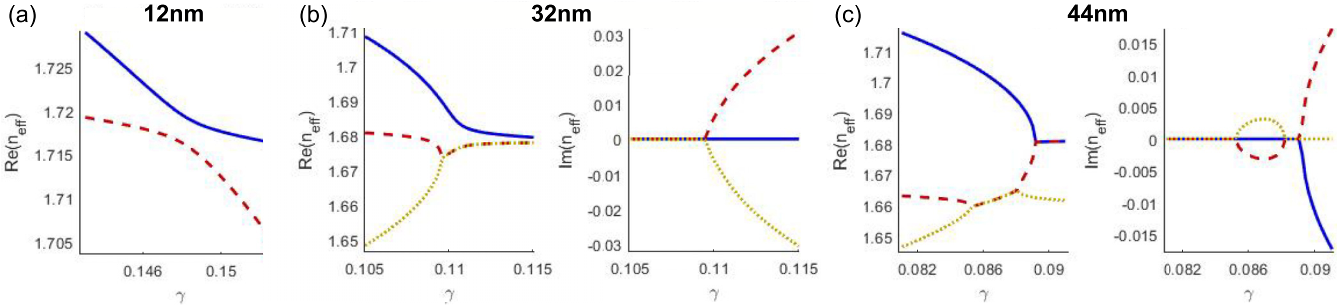

FIG. 5. Eigenvalues obtained from the chiral coupled-mode model for the isolated modes [Eq. (3)], with chiral parameters α and β calculated from the (a) 12-, (b) 32-, and (c) 44-nm-gap simulations at $\gamma = 0$.

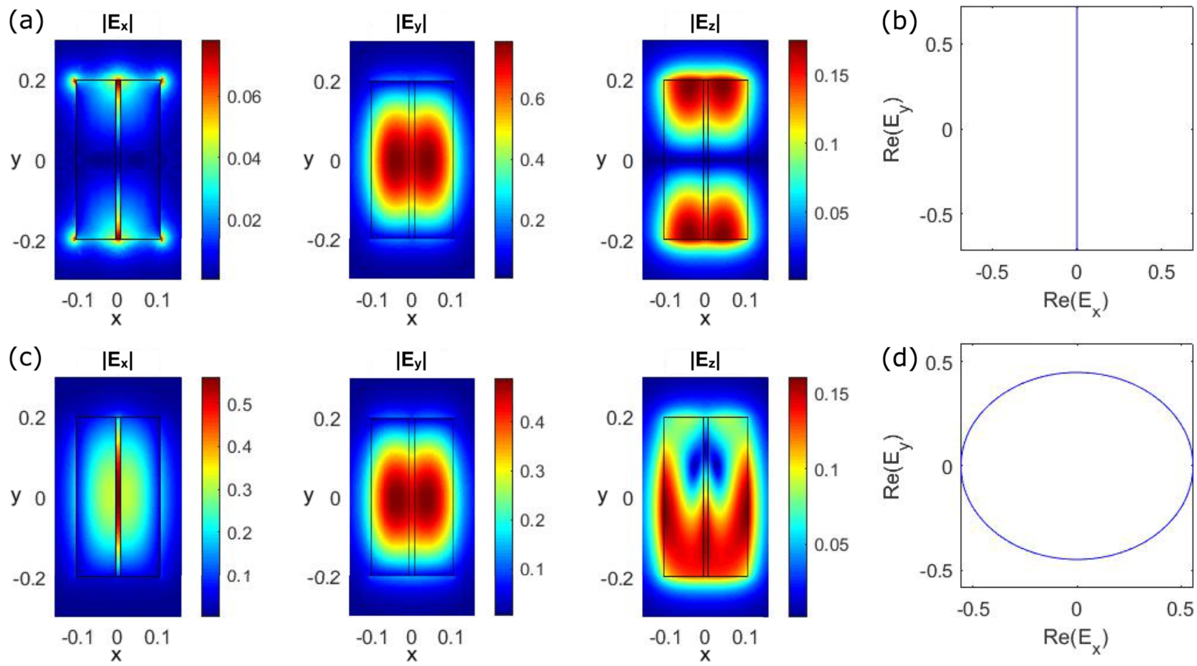

FIG. 6. (a) and (c) Electric-field profile and (b) and (d) central polarization (at $x = y = 0$) of the highest mode TE_{up} for a 12-nm gap at $\gamma = 0.145$ with (a) and (b) $\kappa = 0$ and (c) and (d) $\kappa = 0.012$. The x and y coordinates are expressed in microns and the electric field is in V/m.

The polarization plot of the field at the center of the gap clearly shows a strong ellipticity close to a circular polarization.

This is in good agreement with the eigenvectors $v_{\mathrm{up,up}}$ of the chiral matrix for these two modes [Eq. (5)], in the equal-coupling form, expressed in the basis of the achiral supermodes TE_{up} and TM_{up}:

$$v_{\mathrm{up,up}} = \left(\pm \frac{\beta A + C\alpha}{|\beta A + C\alpha|}, 1 \right)^T . \tag{9}$$

Since α and β are imaginary values, the eigenvectors exhibit an imaginary TE_{up} component and a real TM_{up} component, with the imaginary component taking opposite signs for the two vectors. They thus represent a complex superposition of the TM_{up} and TE_{up} eigenmodes, i.e., an elliptic field polarization. The two eigenvectors have opposite phase differences between the two components due to the $\pm$ sign, similarly to the right and left circularly polarized eigenmodes in a bulk chiral medium.

Around the anticrossing, the magnitude of the x and y electric-field components (at $x = y = 0$) and their phase difference evolve in an interesting manner (Fig. 7). Before the anticrossing, the TE_{up} (blue solid line) and TM_{up} (red dashed line) chiral modes start with y (thin line) and x (thick line) dominant electric-field components, respectively, just like their achiral counterparts. The phase difference between E_x and E_y is already $\pm 90^\circ$ due to chirality [fundamentally due to the i factor in Eq. (1)], resulting in an elongated ellipse. At the anticrossing ($\gamma = 0.148$ for the theoretical dispersion), the electric fields of both modes are equal in magnitude, with phase difference $\pm 90^\circ$, so polarization is nearly circular as observed in Fig. 6 and mentioned above. After the anticrossing, for larger values of γ, their dominant field components are swapped compared to their initial components, with a dominant E_x for TE_{up} and a dominant E_y for TM_{up}. This allows the chiral modes to merge back to a dispersion close to the achiral case, with the proper mode polarizations (TE and TM),

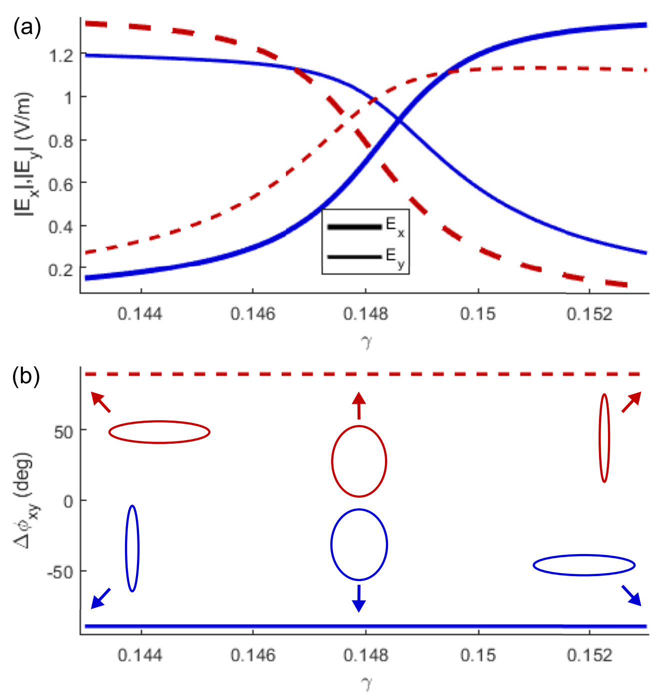

FIG. 7. (a) Module of x (thick lines) and y (thinner lines) electric-field components and (b) phase difference $\Delta\phi_{xy}$ between them for modes TE_{up} (blue solid line) and TM_{up} (red dashed line) for a 12-nm gap. The x and y coordinates are expressed in microns and the electric field is in V/m.

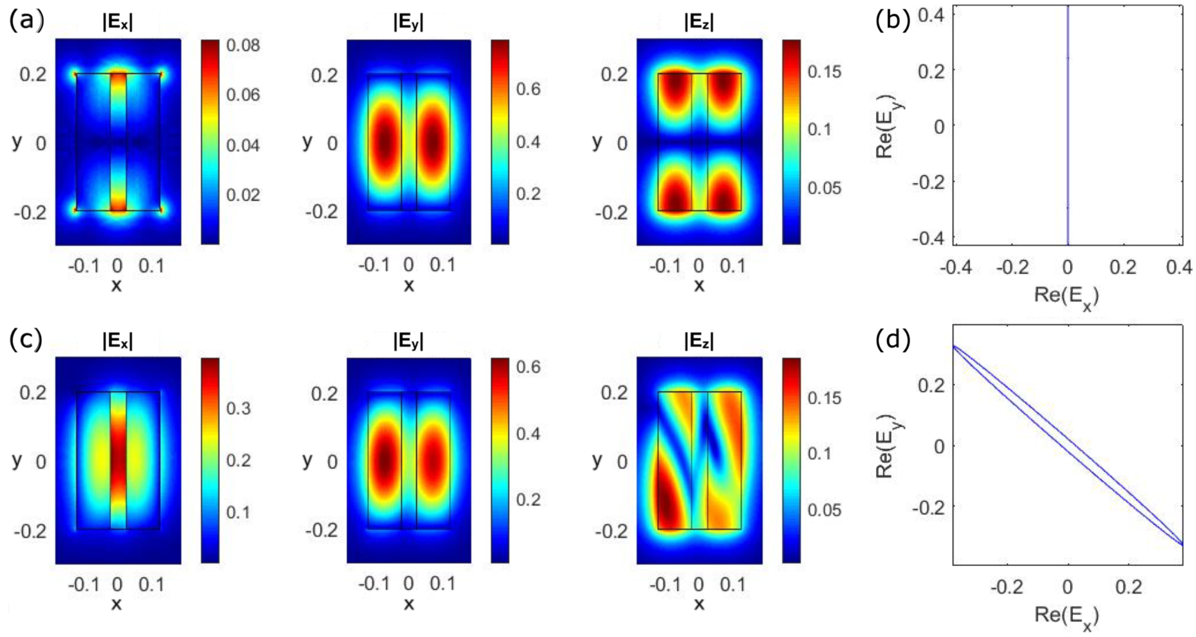

FIG. 8. (a) and (c) Electric-field profile and (b) and (d) central polarization (at $x = y = 0$) of mode $\mathrm{TE_{dn}}$ for a 44-nm gap at $\gamma = 0.086$ with (a) and (b) $\kappa = 0$ and (c) and (d) $\kappa = 0.012$. The x and y coordinates are expressed in microns and the electric field is in V/m.

and the quasicircular polarization evolving into elliptical, and linear further on.

B. Local symmetry breaking

The local symmetry breaking via chirality, with crossing between $\mathrm{TM_{up}}$ and $\mathrm{TE_{dn}}$, also creates hybrid modes. The $\mathcal{PT}$-symmetric profiles and TE polarization of $\mathrm{TE_{dn}}$ can be observed in Figs. 8(a) and 8(b), respectively. With a chiral gap, the local symmetry breaking is manifested through the (slightly) asymmetric E_y field profile in Fig. 8(c). The hybridization is also visible in the tilted quasilinear polarization of the chiral mode [Fig. 8(d)], very distinct from the traditional quasicircular anticrossing modes [Fig. 6(d)].

These results are also modeled with the eigenvectors $v_{\mathrm{dn,up}}$ of the chiral matrix, in the equal-coupling form

$$v_{\mathrm{dn,up}} = \left(\pm \frac{i\alpha}{|\alpha| C}(iA - \gamma), 1\right)^T. \tag{10}$$

Near the EP [as is the case in Fig. 3(a)], the first component of the eigenvectors is almost real, as α is imaginary and γ is close to C, implying that $A = \sqrt{C^2 - \gamma^2}$ is small compared to γ. These vectors, expressed in the basis of the achiral supermodes $\mathrm{TE_{up}}$ and $\mathrm{TM_{dn}}$, thus represent a distinct quasilinear complex superposition of the $\mathrm{TM_{up}}$ and $\mathrm{TE_{dn}}$ eigenmodes, just like the simulated profiles.

The rich variation of the $\mathrm{TM_{up}}$ (red dashed line) and $\mathrm{TE_{dn}}$ (gold dotted line) eigenvectors' polarization across the $\mathcal{PT}$-broken zone is represented in Fig. 9. Figure 9(a) shows that the fields of both modes have equal magnitudes in the $\mathcal{PT}$-broken zone, with equal x (thick lines) and y (thin lines) electric-field modules. The quasilinearity and opposite polarizations of the eigenvectors at the center of the $\mathcal{PT}$-broken zone is due to the local variation of the phase difference between their x and y fields, as evidenced by Fig. 9(b). Both $\mathrm{TM_{up}}$ and $\mathrm{TE_{dn}}$ have a phase difference of -90° before the $\mathcal{PT}$-broken zone and $+90^\circ$ after. However, the phase difference of $\mathrm{TM_{up}}$ transitions to this value through a 180° decrease, thereby passing through $(\pm)180^\circ$ at the center of the zone, whereas $\mathrm{TE_{dn}}$ increases by 180° and passes through 0° at the center. It is exactly this passage through 0° and 180° that provides the two orthogonal,

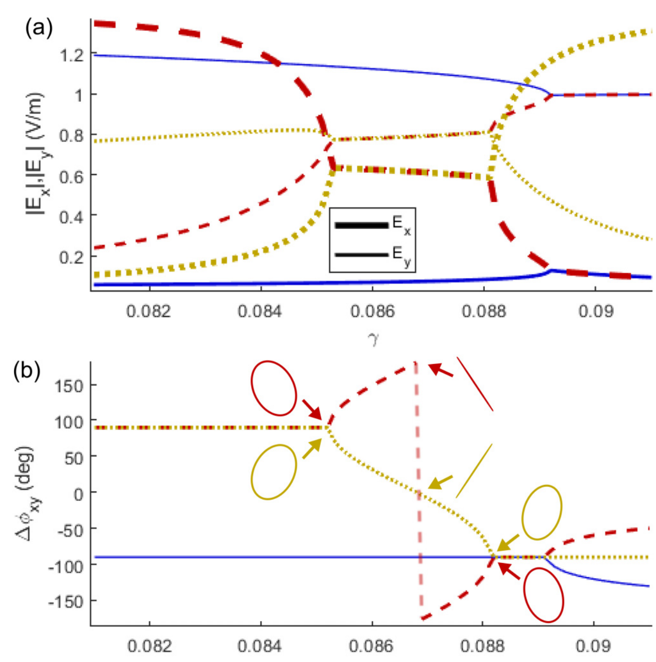

FIG. 9. (a) Module of x (thick lines) and y (thinner lines) electric-field components and (b) phase difference $\Delta\phi_{xy}$ between them for modes $\mathrm{TE_{up}}$ (blue solid line), $\mathrm{TM_{up}}$ (red dashed line), and $\mathrm{TE_{dn}}$ (gold dotted line) for a 44-nm gap.

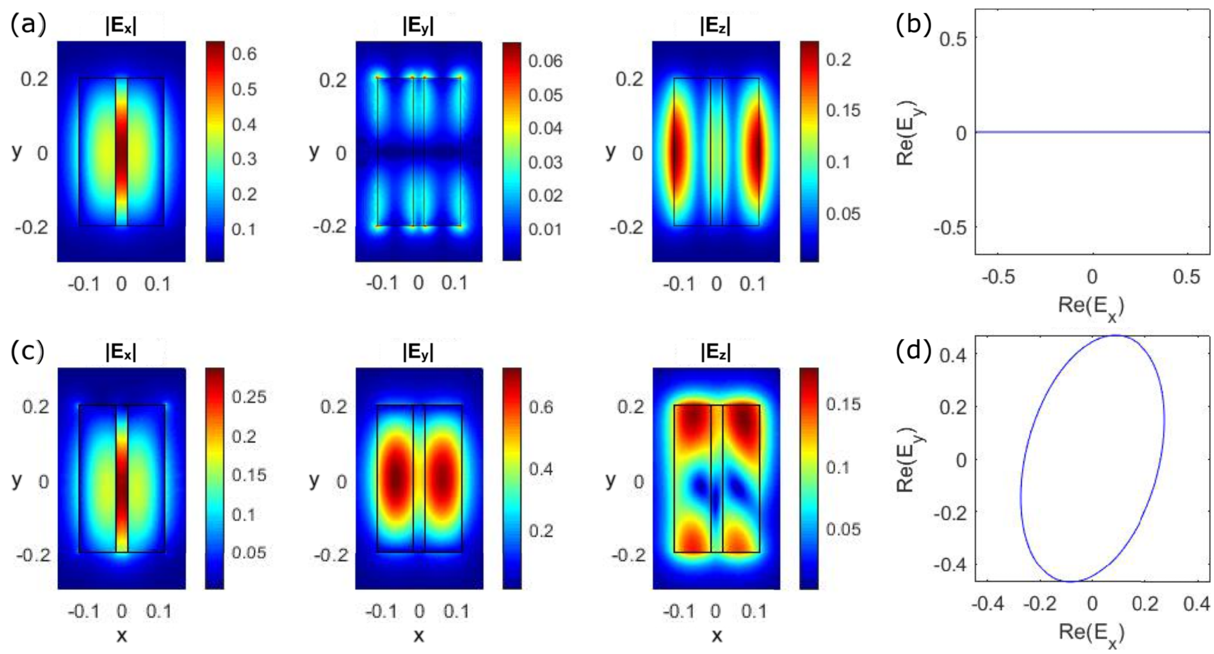

FIG. 10. (a) and (c) Electric-field profile and (b) and (d) central polarization (at $x = y = 0$) of mode TM_{up} for a 32-nm gap at $\gamma = 0.109$ with (a) and (b) $\kappa = 0$ and (c) and (d) $\kappa = 0.012$.

quasilinear, tilted polarizations at the center of the broken zone.

It is interesting to note the qualitative difference (and correspondence) between the anticrossing and local symmetry breaking: For the anticrossing the field components vary, whereas the phase is constant (Fig. 7), while for the local symmetry breaking the field is fairly constant, whereas the phase varies strongly (Fig. 9).

C. Trimodal anticrossing

At the TE EP, TE_{up} and TE_{dn} coalesce and are represented by the same field profile. An intermediate-size gap makes the TM_{up} dispersion cross this EP, so the three modes interact in a hybrid coupling on an equal footing. Figures 10(a) and 10(b) represent the achiral TM_{up} mode, with a dominant x electric-field component, while Figs. 10(c) and 10(d) represent its chiral counterpart [red dashed lines in Figs. 4(c) and 4(e), respectively]. The latter's electric field exhibits an asymmetry in the z component [Fig. 10(c)] and its tilted elliptical polarization suggests that it can be viewed, physically, as a hybrid of the anticrossing and local $\mathcal{PT}$-broken modes [Fig. 10(d)]. Note also that the slot effect is quite large, with a discontinuity of electric field E_x of a factor of approximately 2. This fact strongly advocates for the slot effect as a key element of the attainment of a bulklike chiral sensitivity mentioned earlier, one of the salient features of this study.

VI. CONCLUSION

To summarize, we have shown that introducing a chiral material in the gap of a pair of $\mathcal{PT}$-symmetric waveguides results in a variety of avoided crossing patterns occurring at achiral degeneracies in the mode dispersion, accessible through modulation of the $\mathcal{PT}$ landscape with a proper initial waveguide design. For narrow gaps, an anticrossing appears in the chiral mode dispersion and the polarization of the affected modes becomes quasicircular, much as in the bulk. Medium-size gaps yield a trimodal anticrossing that appears to display the same sensitivity as a fully homogeneous chiral medium, an interesting feature for which the slot effect has been invoked and which could be exploited in integrated chiral sensing applications. Finally, for wide gaps, chirality brings about a local broken-symmetry zone followed by symmetry recovery with an inverted EP. In the gap the polarization of the locally broken modes varies strongly, which can lead to interesting switching opportunities. The coupled-mode model developed in this work reproduces these features in much detail, enough to form the basis for quantitative designs and the study of novel geometries, for example, with higher-order EPs, or other types of $\mathcal{PT}$ symmetry (anti-$\mathcal{PT}$ or gainless $\mathcal{PT}$, for example). The model further elucidates that gain and loss not only are useful to obtain degeneracy, but are fundamental to obtain the local breaking effect.

ACKNOWLEDGMENTS

A.D.C. acknowledges support from the Fund for Scientific Research F.R.S.-FNRS through a FRIA grant.

APPENDIX A: AVOIDED CROSSINGS FOR COMPLEX CHIRALITY PARAMETER

The chirality parameter κ controls the nature of the chiral coupling. If its value is changed from real to imaginary, the types of avoided crossings are swapped: An anticrossing appears between modes of opposite parity (under the TE EP), while a $\mathcal{PT}$-broken zone appears at crossings between modes of the same parity (above the TE EP). If κ is complex with real and imaginary parts of the same order, a hybrid avoided

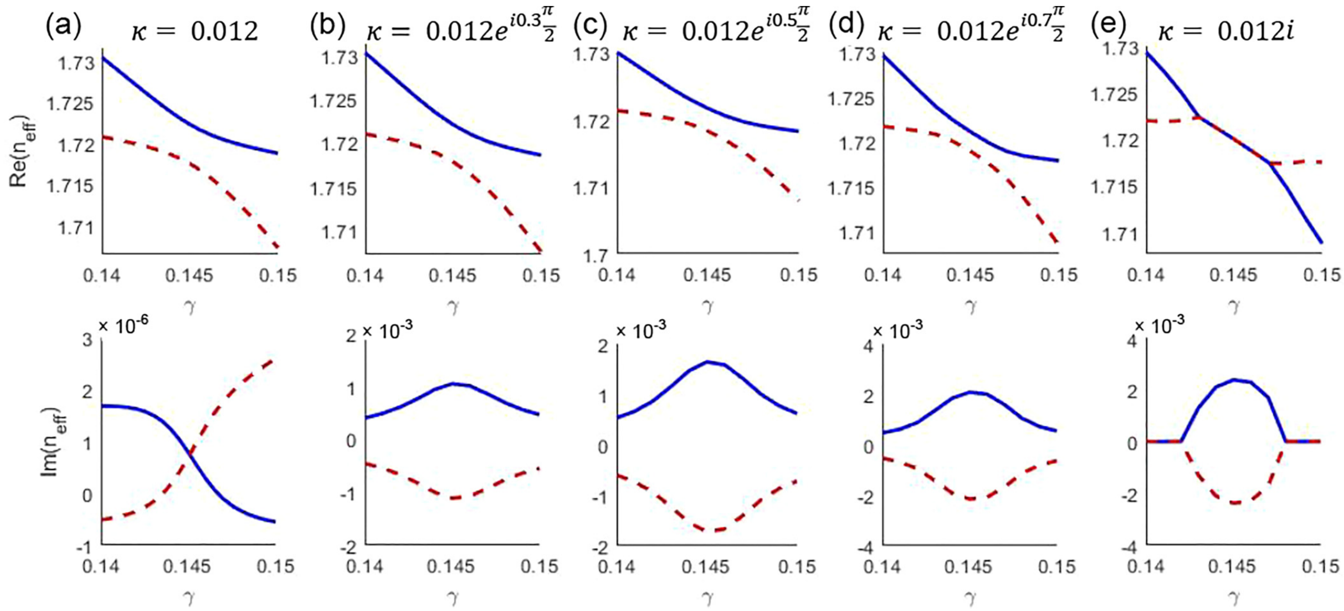

FIG. 11. Real (top) and imaginary (bottom) dispersions of modes TE_{up} (blue solid line) and TM_{up} (red dashed line) for a 12-nm chiral gap with (a) $\kappa = 0.012$, (b) $\kappa = 0.012e^{i0.3\pi/2}$, (c) $\kappa = 0.012e^{i0.5\pi/2}$, (d) $\kappa = 0.012e^{i0.7\pi/2}$, and (e) $\kappa = 0.012i$.

crossing appears as both effects compete in the alteration of the dispersion (see Fig. 11).

APPENDIX B: COUPLED-MODE-THEORY PARAMETERS

The coupled-mode theory, expressed in the isolated modes basis as in Eq. (3), involves achiral as well as chiral coefficients. This Appendix describes their calculation methods.

The achiral coefficients are based on the mode dispersions for achiral gaps. The effective indices of the isolated TE and TM modes without any coupling, n_{TE} and n_{TM}, are the value of n_{eff} at the EP for the relevant polarization. The mode couplings C_{TE} and C_{TM} are approximated by dividing the difference between the effective indices of the upper and lower fork modes for each polarization, divided by 2:

$$C_{TE,TM} = [n_{eff}(TE, TM_{up}) - n_{eff}(TE, TM_{up})]/2. \tag{B1}$$

As mentioned in Sec. IV, the effective imaginary refractive indices γ_{TE} and γ_{TM} perceived by the isolated TE and TM modes are proportional to the material imaginary refractive index γ. These proportionality factors are the confinement factors of each polarization, which we call F_{TE} and F_{TM}: $\gamma_{TE} = F_{TE}\gamma$ and $\gamma_{TM} = F_{TM}\gamma$. The confinement factors are deduced from the values of C and γ_{EP} for each polarization. $\mathcal{PT}$-symmetry theory states that TE and TM exceptional points occur when $\gamma_{TE} = C_{TE}$ and $\gamma_{TM} = C_{TM}$. We have access to the value of γ, the material's imaginary index, at each exceptional point, as well as C_{TE} and C_{TM} from the method described by Eq. (B1). It then follows that, for each polarization,

$$F = \gamma_{eff}(EP)/\gamma(EP), \tag{B2}$$

where γ_{eff} is the effective imaginary refractive index γ_{TE} or γ_{TM} and γ is the material imaginary refractive index. The values of n_{TE}, n_{TM}, C_{TE}, C_{TM}, F_{TE}, and F_{TM} are included in Table I.

To obtain the chiral couplings α and β used in our model, we make use of an adaptation of the theory presented in Ref. [26], with overlap integrals written as I_{mn} in Sec. IV. Since the general supermode model is quite complex, we use its expression at $\gamma = 0$ to determine α and β. The coupling matrix of this model is

$$\begin{bmatrix} n_{TE} + C_{TE} & 0 & \beta + \alpha & 0 \\ 0 & n_{TE} - C_{TE} & 0 & \beta - \alpha \\ \beta^* + \alpha^* & 0 & n_{TM} + C_{TM} & 0 \\ 0 & \beta^* - \alpha^* & 0 & n_{TM} - C_{TM} \end{bmatrix} \tag{B3}$$

[see Eq. (4)]. It can be seen that the overlap integral I_{13} between TE_{up} and TM_{up} gives $\beta + \alpha$ and the overlap integral I_{24} between TE_{dn} and TM_{dn} gives $\beta - \alpha$. It is then easily obtained that

$$\alpha = \tfrac{1}{2}(I_{13} - I_{24}), \quad \beta = \tfrac{1}{2}(I_{13} + I_{24}). \tag{B4}$$

Their values are included in Table II.

APPENDIX C: MAGNETIC-FIELD MODE PROFILES

Below are the magnetic-field profiles for the modes presented in Sec. V.

1. Anticrossing

Modes TE_{up} and TM_{up} couple under the influence of chirality to form two quasicircular polarization modes at the anticrossing (for polarization, see Fig. 6), with similar magnitudes of H_x and H_y (see Fig. 12).

2. Local symmetry breaking

At the crossing between the achiral dispersions of modes TM_{up} and TE_{dn}, the chiral structure admits two $\mathcal{PT}$-broken modes with left-right asymmetric field profiles (see Fig. 13).

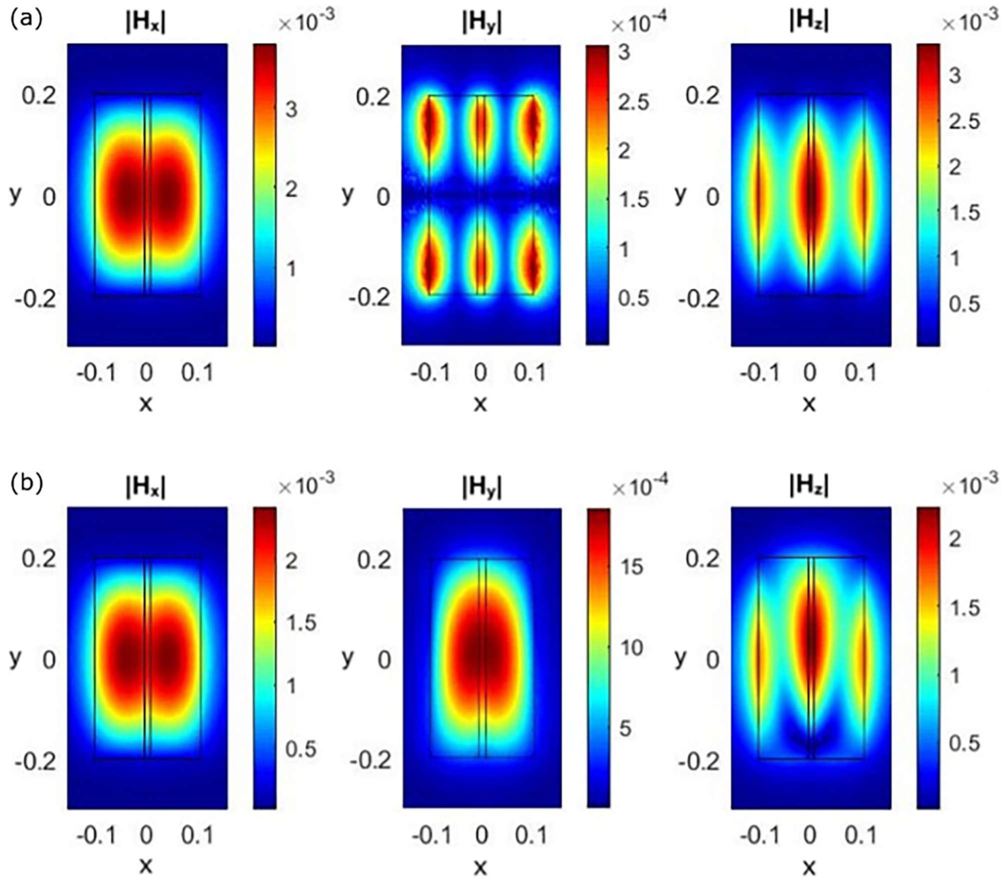

FIG. 12. Magnetic-field profile of the highest mode $\mathrm{TE_{up}}$ for a 12-nm gap at $\gamma = 0.145$ with (a) $\kappa = 0$ and (b) $\kappa = 0.012$. The x and y coordinates are expressed in microns and the magnetic field is in A/m.

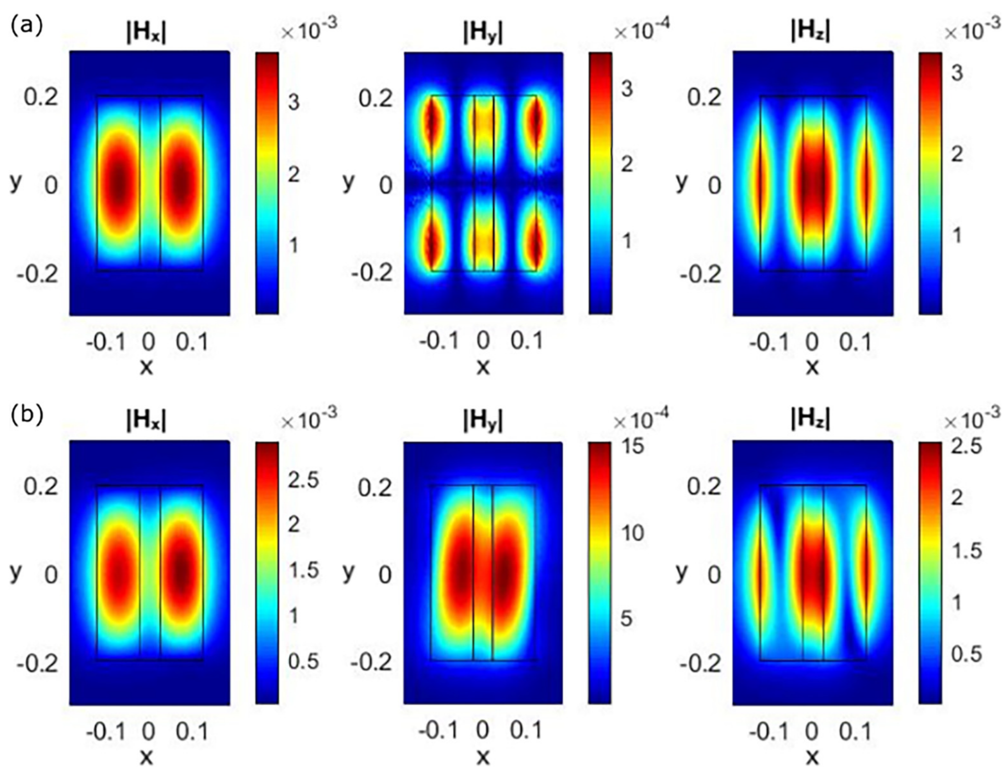

FIG. 13. Magnetic-field profile of mode $\mathrm{TE_{dn}}$ for a 44-nm gap at $\gamma = 0.086$ with (a) $\kappa = 0$ and (b) $\kappa = 0.012$. The x and y coordinates are expressed in microns and the magnetic field is in A/m.

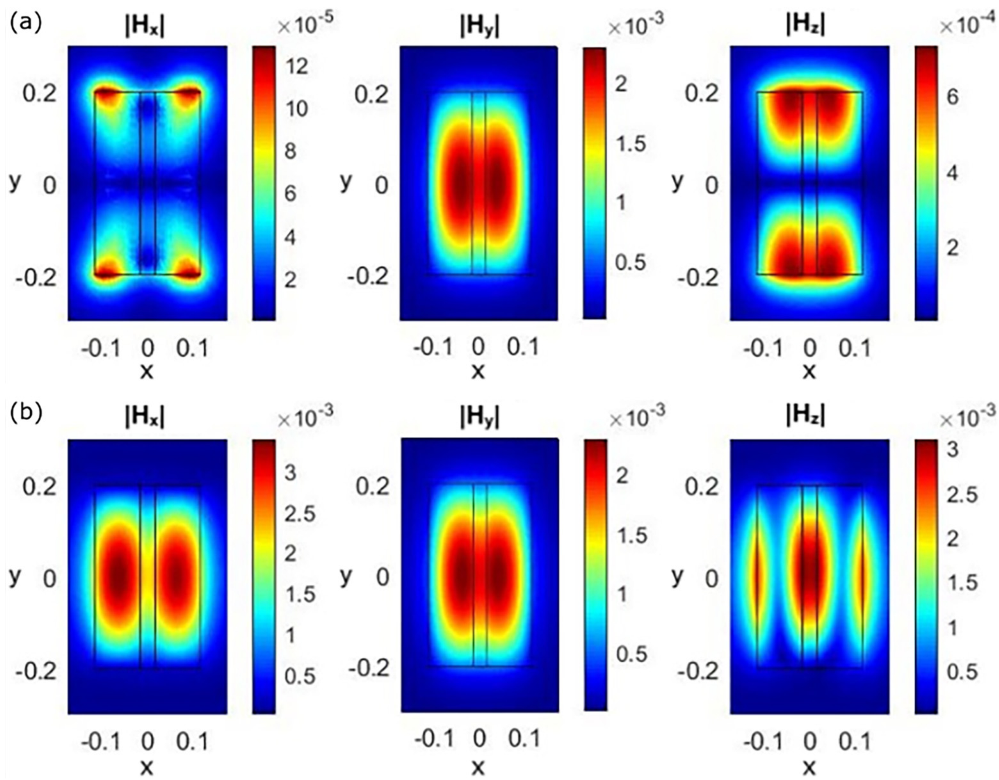

FIG. 14. Magnetic-field profile of mode TM_{up} for a 32-nm gap at $\gamma = 0.109$ with (a) $\kappa = 0$ and (b) $\kappa = 0.012$. The x and y coordinates are expressed in microns and the magnetic field is in A/m.

3. Trimodal anticrossing

A hybrid coupling occurs between TE_{up}, TE_{dn}, and TM_{up} modes at the EP. Coupling the TE modes with TM_{up} through chirality results in a slightly left-right asymmetric field profile (see Fig. 14).

[1] C. Rüter, K. Makris, R. El-Ganainy, D. Christodoulides, M. Segev, and D. Kip, Observation of paritytime symmetry in optics, Nat. Phys. **6**, 192 (2010).

[2] H. Ramezani, T. Kottos, R. El-Ganainy, and D. N. Christodoulides, Unidirectional nonlinear $\mathcal{PT}$-symmetric optical structures, Phys. Rev. A **82**, 043803 (2010).

[3] H. Benisty, A. Lupu, and A. Degiron, Transverse periodic $\mathcal{PT}$ symmetry for modal demultiplexing in optical waveguides, Phys. Rev. A **91**, 053825 (2015).

[4] J. Petráček, in *19th International Conference on Transparent Optical Networks (ICTON), 2017* (IEEE, Piscataway, 2017), pp. 1–4.

[5] R. Kolkowski and A. F. Koenderink, Lattice resonances in optical metasurfaces with gain and loss, Proc. IEEE **108**, 795 (2019).

[6] P. Markoš and V. Kuzmiak, Resonant scattering from a two-dimensional honeycomb $\mathcal{PT}$ dipole structure, Phys. Rev. A **97**, 053807 (2018).

[7] Y. Tian, Z. Tan, W. Zhang, X. Han, and C. Cho, Edge states in a non-Hermitian chiral lattice, Int. J. Mech. Sci. **224**, 107352 (2022).

[8] H. Benisty, A. Degiron, A. Lupu, A. De Lustrac, S. Chénais, S. Forget, M. Besbes, G. Barbillon, A. Bruyant, S. Blaize, and G. Lérondel, Implementation of PT symmetric devices using plasmonics: Principle and applications, Opt. Express **19**, 18004 (2011).

[9] Y. Moritake and M. Notomi, Switchable unidirectional radiation from huygens dipole formed at an exceptional point in non-Hermitian plasmonic systems, ACS Photonics **10**, 667 (2023).

[10] Y. D. Chong, L. Ge, and A. D. Stone, $\mathcal{PT}$-symmetry breaking and laser-absorber modes in optical scattering systems, Phys. Rev. Lett. **106**, 093902 (2011).

[11] L. Feng, R. El-Ganainy, and L. Ge, Non-Hermitian photonics based on parity–time symmetry, Nat. Photonics **11**, 752 (2017).

[12] H. Hodaei, A. Hassan, S. Wittek, H. Garcia-Gracia, R. El-Ganainy, D. Christodoulides, and M. Khajavikhan, Enhanced sensitivity at higher-order exceptional points, Nature (London) **548**, 187 (2017).

[13] *Parity-Time Symmetry and its Applications*, edited by D. Christodoulides and J. Yang, Springer Tracts in Modern Physics Vol. 280 (Springer, Singapore, 2018).

[14] M.-A. Miri and A. Alù, Exceptional points in optics and photonics, Science **363**, eaar7709 (2019).

[15] Y. Jian, Y. Wang, Z. Guo, S. Hu, B. Wu, Y. Yang, and H. Chen, External excitation enabled chirality reversal of exceptional points in an effective anti-PT-symmetric non-Hermitian system, Appl. Phys. Lett. **123**, 141702 (2023).

[16] J. Wiersig, Prospects and fundamental limits in exceptional point-based sensing, Nat. Commun. **11**, 2454 (2020).

[17] K. Takata, N. Roberts, A. Shinya, and M. Notomi, Imaginary couplings in non-Hermitian coupled-mode theory: Effects on exceptional points of optical resonators, Phys. Rev. A **105**, 013523 (2022).
[18] M. Born, On the theory of optical activity. I. General theory of a system of coupled isotropic oscillators. II. molecules with a binary axis of symmetry, Proc. R. Soc. London Ser. A **150**, 84 (1936).
[19] M. Hentschel, M. Schäferling, X. Duan, H. Giessen, and N. Liu, Chiral plasmonics, Sci. Adv. **3**, e1602735 (2017).
[20] M. L. Nesterov, X. Yin, M. Schäferling, H. Giessen, and T. Weiss, The role of plasmon-generated near fields for enhanced circular dichroism spectroscopy, ACS Photonics **3**, 578 (2016).
[21] T. V. Raziman, R. H. Godiksen, M. A. Müller, and A. G. Curto, Conditions for enhancing chiral nanophotonics near achiral nanoparticles, ACS Photonics **6**, 2583 (2019).
[22] F. Graf, J. Feis, X. Garcia-Santiago, M. Wegener, C. Rockstuhl, and I. Fernandez-Corbaton, Achiral, helicity preserving, and resonant structures for enhanced sensing of chiral molecules, ACS Photonics **6**, 482 (2019).
[23] E. Pedrueza-Villalmanzo, F. Pineider, and A. Dmitriev, Perspective: Plasmon antennas for nanoscale chiral chemistry, Nanophotonics **9**, 481 (2020).
[24] S. Yu, X. Piao, and N. Park, Chirality in non-Hermitian photonics, Curr. Opt. Photon. **3**, 275 (2019).
[25] J. Mun, M. Kim, Y. Yang, T. Badloe, J. Ni, Y. Chen, C.-W. Qiu, and J. Rho, Electromagnetic chirality: From fundamentals to nontraditional chiroptical phenomena, Light Sci. Appl. **9**, 139 (2020).
[26] P. Pelet and N. Engheta, Coupled-mode theory for chirowaveguides, J. Appl. Phys. **67**, 2742 (1990).
[27] M. Saadoun and N. Engheta, Theoretical study of variation of propagation constant in a cylindrical waveguide due to chirality: Chiro-phase shifting, IEEE Trans. Microw. Theory Tech. **42**, 1690 (1994).
[28] E. O. Kamenetskii, Mode interactions in chirowaveguides, J. Appl. Phys. **79**, 8899 (1996).
[29] V. Abramov, O. Osipov, D. Klyuev, and A. Neshcheret, in *International Conference on Information Technology and Nanotechnology (ITNT) 2021* (IEEE, Piscataway, 2021), pp. 1–6.
[30] B. Peng, Ş. K. Özdemir, M. Liertzer, W. Chen, J. Kramer, H. Yılmaz, J. Wiersig, S. Rotter, and L. Yang, Chiral modes and directional lasing at exceptional points, Proc. Natl. Acad. Sci. USA **113**, 6845 (2016).
[31] A. Hashemi, S. M. Rezaei, S. K. Özdemir, and R. El-Ganainy, New perspective on chiral exceptional points with application to discrete photonics, APL Photonics **6**, 040803 (2021).
[32] J. Ren, S. Franke, and S. Hughes, Quasinormal mode theory of chiral power flow from linearly polarized dipole emitters coupled to index-modulated microring resonators close to an exceptional point, ACS Photonics **9**, 1315 (2022).
[33] S. Yu, H. S. Park, X. Piao, B. Min, and N. Park, Low-dimensional optical chirality in complex potentials, Optica **3**, 1025 (2016).
[34] S. Yu, X. Piao, and N. Park, Acceleration toward polarization singularity inspired by relativistic $E \times B$ drift, Sci. Rep. **6**, 37754 (2016).
[35] M. Lawrence, N. Xu, X. Zhang, L. Cong, J. Han, W. Zhang, and S. Zhang, Manifestation of PT symmetry breaking in polarization space with terahertz metasurfaces, Phys. Rev. Lett. **113**, 093901 (2014).
[36] I. Katsantonis, S. Droulias, C. M. Soukoulis, E. N. Economou, and M. Kafesaki, $\mathcal{PT}$-symmetric chiral metamaterials: Asymmetric effects and $\mathcal{PT}$-phase control, Phys. Rev. B **101**, 214109 (2020).
[37] I. Katsantonis, S. Droulias, C. M. Soukoulis, E. N. Economou, and M. Kafesaki, Scattering properties of PT-symmetric chiral metamaterials, Photonics **7**, 43 (2020).
[38] S. Droulias, I. Katsantonis, M. Kafesaki, C. M. Soukoulis, and E. N. Economou, Chiral metamaterials with PT symmetry and beyond, Phys. Rev. Lett. **122**, 213201 (2019).
[39] I. Katsantonis, S. Droulias, C. M. Soukoulis, E. N. Economou, T. P. Rakitzis, and M. Kafesaki, Chirality sensing employing parity-time-symmetric and other resonant gain-loss optical systems, Phys. Rev. B **105**, 174112 (2022).
[40] E. Hendry, R. V. Mikhaylovskiy, L. D. Barron, M. Kadodwala, and T. J. Davis, Chiral electromagnetic fields generated by arrays of nanoslits, Nano Lett. **12**, 3640 (2012).
[41] J. S. Choi and M. Cho, Limitations of a superchiral field, Phys. Rev. A **86**, 063834 (2012).
[42] M. Decker, M. Ruther, C. E. Kriegler, J. Zhou, C. M. Soukoulis, S. Linden, and M. Wegener, Strong optical activity from twisted-cross photonic metamaterials, Opt. Lett. **34**, 2501 (2009).
[43] M. Decker, R. Zhao, C. M. Soukoulis, S. Linden, and M. Wegener, Twisted split-ring-resonator photonic metamaterial with huge optical activity, Opt. Lett. **35**, 1593 (2010).
[44] R. Zhao, L. Zhang, J. Zhou, T. Koschny, and C. M. Soukoulis, Conjugated gammadion chiral metamaterial with uniaxial optical activity and negative refractive index, Phys. Rev. B **83**, 035105 (2011).
[45] N. X. A. Rivolta and B. Maes, Symmetry recovery for coupled photonic modes with transversal PT symmetry, Opt. Lett. **40**, 3922 (2015).
[46] J. Kullig, D. Grom, S. Klembt, and J. Wiersig, Higher-order exceptional points in waveguide-coupled microcavities: Perturbation induced frequency splitting and mode patterns, Photon. Res. **11**, A54 (2023).
[47] V. R. Almeida, Q. Xu, C. A. Barrios, and M. Lipson, Guiding and confining light in void nanostructure, Opt. Lett. **29**, 1209 (2004).
[48] M. A. Ettabib, A. Marti, Z. Liu, B. M. Bowden, M. N. Zervas, P. N. Bartlett, and J. S. Wilkinson, Waveguide enhanced raman spectroscopy for biosensing: A review, ACS Sensors **6**, 2025 (2021).